



Silver nanoparticles-sensitized cobalt complex for highly-efficient photocatalytic activity

Jingpei Huo, Heping Zeng*

State Key Laboratory of Luminescent Materials and Devices, Institute of Functional Molecules, School of Chemistry and Chemical Engineering, South China University of Technology, Guangzhou, 510641, PR China



ARTICLE INFO

Article history:

Received 14 April 2016

Received in revised form 12 June 2016

Accepted 18 June 2016

Available online 19 June 2016

Keywords:

Photocatalytic hydrogen production

Metal complex

Silver nanoparticles

ABSTRACT

Triphenylamine functionalized bithiazole-cobalt complex (**Co-2TPABTz**) sensitized by Ag nanoparticles (NPs) exhibit highly efficient photocatalytic hydrogen generation. The resulting composite **3** showed excellent photocatalytic activity ($20.65 \text{ mmol h}^{-1} \text{ g}^{-1}$) under visible light illumination, and maintained outstanding long-term stability after eight-cycle tests (32 h) as well.

© 2016 Elsevier B.V. All rights reserved.

1. Introduction

The development of reliable and environmentally friendly approaches for energy conversion is one of the key challenges that our society is facing [1,2]. In addition to solving the global energy need and environmental pollution, hydrogen (H_2) has attracted much attention for its potential to replace fossil fuels [3,4]. Currently, however, production of H_2 is mostly based on fossil fuels, accompanied with high energy consumption [5,6]. Among a variety of approaches, photocatalytic H_2 evolution is of particular interest because of its simplicity, low-cost operation and the use of water [7,8].

Recently, metal (M) complexes have emerged as promising candidates for the synthesis of nano-materials, because of their unique structure, atomic metal dispersion and textural properties [9,10]. M-complexes also known as porous coordination polymers, makes it an ideal platform for photochemical water splitting thanks to the enhanced charge carrier mobility and large surface area [11,12]. Likewise, using **Co-2TPABTz** as a modular organic building block [13], that may be coupled with nanoparticles (NPs) or other molecular catalysts interchangeably to produce functional materials [14,15].

To date, NPs have been combined with photocatalysts to improve their activity in the visible spectra [16,17]. Among various candidates, Ag NPs is one of the most effective sensitizers in photo-

catalytic H_2 evolution [18,19], due to their relative low cost, facile preparation and high efficiency under near-neutral pH conditions [20,21]. It is also proved that Ag NPs displays strong surface plasmon resonance (SPR) effect even its size decreases to below 10 nm [20,22]. As for their promising light-harvesting and electron transfer properties, Ag NPs have been successfully incorporated with M-complexes and underexplored in photocatalytic applications [11,23]. Herein, we take advantage of a new photocatalytic system (**Scheme S1**) composed of Ag NPs and a cobalt molecular catalyst (**Co-2TPABTz**) to study the overall photo-induced catalytic process [13,24–26], and it exhibit efficient photocatalytic activity and a high level of stability under visible light irradiation ($\lambda > 420 \text{ nm}$). In addition, this work can provide some new insights for the smart design and preparation of inexpensive and high-efficiency photocatalysts.

2. Experimental

2.1. Materials

All the chemical solvents and reagents were analytical grade and used without additional purification [27]. Among them, Hexadecyltrimethylammonium bromide (CTAB, $\geq 99.0\%$), silver nitrate (AgNO_3 , $\geq 99.0\%$), ascorbic acid ($\text{C}_6\text{H}_8\text{O}_6$, $\geq 98.0\%$) and sodium hydroxide (NaOH , $\geq 98.0\%$) was purchased from Sinopharm Chemical Reagent Co. Ltd [28]. Tetrabutylammonium hexafluorophosphate (TBAPF_6 , $\geq 99.0\%$) was provided from J&K Chemical Ltd. The complex **Co-2TPABTz** was synthesized and characterized as previously described (**Scheme S1**) [13]. Besides, Nafion (5%) was purchased

* Corresponding author.

E-mail address: hpzeng@scut.edu.cn (H. Zeng).

from J&K Chemical Ltd. E-pure deionized (DI) water (resistivity >18 M Ω cm) was supplied by a Millipore Milli-Q system.

2.2. Instruments

Crystallographic information for the as-synthesized samples was obtained on an X-ray diffractometer (Bruker, Germany) with mono-chromatized Cu K α radiation ($\lambda = 0.15406$ nm).

The detailed morphology and structure of the products were recorded by transmission electron microscopy (TEM), high resolution transmission electron microscope (HR-TEM) and selected area electron diffraction (SAED), on a JEM-2100 apparatus with an accelerating voltage of 200 kV. Energy-dispersive X-ray (EDX) spectroscopy was also given from an EDAX detector performed on the same HR-TEM.

The chemical compositions and surface states of those samples were probed with an X-ray photoelectron spectroscopy (XPS, Axis Ultra DLD, Kratos) instrument.

The actual chemical compositions of the as-prepared products after the thorough purification were performed using an inductively coupled plasma atomic emission spectrometry (ICP-AES, Prodigy, Leeman, LABS, Inc.).

The Brunauer-Emmett-Teller (BET) specific surface area of as-synthesized photocatalysts was evaluated at 77 K with a Quantochrome NOVA 1200e instrument.

Raman spectroscopy was measured by performed with a Renishaw 514.5 nm argon laser.

Time-resolved photoluminescence decay spectra tests were carried out at room temperature using an Edinburgh FLS 920 Fluorescence spectrometer.

Photoelectrochemical (PEC) and electrochemical impedance spectra (EIS) measurements were carried out by electrochemical analyzer (CHI660C Instruments, Shanghai, China) with a conventional three-electrode system [29,30]. Prior to these experiments, the film electrodes of Ag NPs loaded **Co-2TPABTz** were prepared at first. The as-prepared sample was employed as working electrode, the counter electrode and the reference electrode were platinum mesh and a Ag/AgCl (saturated KCl) separately. Lactic acid (10%, v/v) was mixed with Na₂SO₄ (0.5 mol L⁻¹) aqueous solution as the supporting electrolyte [31,32].

The measured potentials versus the Ag/AgCl reference electrode were converted to the reversible hydrogen electrode (RHE) scale via the Nernst equation:

$$E_{\text{RHE}} = E_{\text{Ag/AgCl}}^0 + E_{\text{Ag/AgCl}} + 0.059\text{pH}$$

where E_{RHE} is the converted potential versus RHE, $E_{\text{Ag/AgCl}}$ is the experimental potential measured against the Ag/AgCl reference electrode, and is the standard potential of Ag/AgCl (saturated KCl) at room temperature (i.e., 0.197) [33].

Both linear sweep voltammetry (LSV) and photocurrent-time response (I - t) experiments were conducted in a three-electrode system, and the scan rate was 20 mV s⁻¹. The photocurrent densities produced at a bias of -0.4 V versus RHE in the dark and visible-light irradiation ($\lambda > 420$ nm, light on/off cycles: 20 s). The photo-stability measurement was performed under the same condition. Besides, EIS spectrum of the as-prepared samples and **Co-2TPABTz** were measured by following the identical procedure according to the previous reference [13].

UV-vis spectra were measured using a Hitachi U-3010 absorption spectrophotometer in the range of 300–700 nm. Photoluminescence (PL) spectra were carried out by Hitachi F-4500 fluorescence spectrophotometer, with the excitation wavelength of 410 \pm 5 nm. Besides, the solid fluorescence quantum yields (ϕ_{PL}) values were achieved from a calibrated integrating sphere system ($\lambda_{\text{ex}} = 415$ nm) [34].

Electron spin resonance (ESR) spectra were recorded with a ESR spectrometer (Bruker EMX-10). Before testing, the as-synthesized samples respectively immersed in an aqueous solution (2 mL) including lactic acid (10%, v/v) were added to the cell, evacuated at 77 K to remove dissolved oxygen, and then illuminated for 30 min under visible light ($\lambda > 420$ nm) at room temperature [35]. Meanwhile, ESR spectra for the composite **3** without visible-light illumination (Control) was shown in Fig. S9g.

Cyclic voltammetry (CV) was also measured by electrochemical analyzer (CHI660C Instruments, Shanghai, China) consisting of a standard three-electrode setup as mentioned above [31,32]. TBAPF₆ and ferrocenium-ferrocene (Fc⁺/Fc) worked as the supporting electrolyte and internal standard, respectively. All the potentials were determined at a scan rate of 100 mV s⁻¹ for oxidation in N₂-purged dichloromethane and 100 mV s⁻¹ for reduction in acetonitrile.

2.3. Preparation of silver nanoparticles (Ag NPs) [36,37]

In a typical procedure, CTAB (20.0 mmol, 7.2890 g) and AgNO₃ (4.5 mmol, 0.7644 g) were dissolved in DI water (20 mL) with violent stirring in a flask (50 mL). Hereafter, a total of ascorbic acid (2 mL, 0.5 M), NaOH (0.5 mL, 2.5 M) and NaBH₄ (1 mL, 0.5 M) were dispersed in the above solution with continuous vigorous stirring. All the washing and surface modification processes were carried out with an argon-filled glovebox. All the solvents were degassed under argon for 1 h. After half an hour, the reaction solution was washed with ethanol and water (v/v = 1:3) for three times and centrifuged at 20,000 rpm for 60 min. The resulting solution was dialyzed with DI water in a dialysis bag (retain molecular weight 1500 Da) for 24 h.

2.4. Typical procedure for the synthesis of composites 1–5 [13,28]

Briefly, an appropriate amount of **Co-2TPABTz** was added to toluene (20 mL) and sonicated for 30 min to make them disperse totally. Afterwards, the resultant suspension was dropwise added into the Ag NPs solution (50 mL) with vigorous magnetic stirring in a dark environment at room temperature. And then the resultant mixture was under constant magnetic stirring, aged overnight. After volatilization of the toluene, the resulting powder was washed with ethanol and DI water for three times, and dried under vacuum at 80 °C for 12 h to acquire the Ag NPs hybridized complex samples. Moreover, the nominal weight ratios of Ag NPs were from 1 to 20 wt% in the composites 1–5.

2.5. Band gap calculation [38,39]

The energy band gap (E_g) of the samples was calculated from the absorption edge of Tauc plot, using the Tauc expression, given below,

$$(\alpha h\nu) = A(h\nu - E_g)^n$$

Where α is the absorption co-efficient, h is Plank constant, ν is the wavenumber (λ). The value of $h\nu$ is obtained from the λ . E_g is determined from the intercept of the extrapolated linear part of the curve with the energy axis. In another case, the valence band (VB) top position was measured from the VB XPS plot and conduction band (CB) bottom was calculated by subtracting the E_g . Therefore, the VB and CB potentials of **Co-2TPABTz** and Ag NPs were listed in Table S2.

2.6. Photocatalytic experiments [25,26]

Typical photocatalytic experiments were set up as follows. Photocatalytic performances of as-synthesized samples were evaluated in a closed gas circulation system equipped with a Pyrex glass reaction cell. Briefly, a total of each photocatalyst (0.05 g) was respectively loaded into a mixture of lactic acid (10 mL) and water (90 mL) in the reactor under magnetic stirring. The reactor was placed in a thermoregulated rack at room temperature with stirring and irradiated using a high-pressure Xe lamp (300 W) with a UV-cutoff filter. In addition, high purity (99.999%) N₂ carrier gas was employed.

2.7. H₂ detected by online gas chromatography (GC) [40]

Generated H₂ was characterized by GC analysis (GC7900, Tian Mei, Shanghai), equipped with a 5 Å molecular sieve column and a thermal conductivity detector (TCD). The retention time of H₂ was about 0.9 min in the same condition. First of all, an H₂ calibration curve was obtained by high purity (99.999%) H₂. And then the evolved H₂ from the photocatalytic measurement was injected into the online GC to get the H₂ peak area. Based on the previous calibration curve, the actual volume of H₂ for those samples was calculated.

2.8. Determination of AQY values [2,41]

Apparent quantum efficiency (AQY) was measured using various monochromatic lights with different band-pass filters ($\lambda = 420, 450, 480, 510, 540, 570, 600, 630, 660$ and 690 nm) and an irradiatometer. The AQY was then estimated by the following formula.

$$\text{AQY\%} = \frac{\text{Number of reacted electrons}}{\text{Number of incident photons}} \times 100\%$$

$$= \frac{2 \times \text{Number of evolved H}_2 \text{ molecules}}{\text{Number of incident photons}} \times 100\%$$

3. Results and discussion

3.1. Characterization

XRD measurements are employed to analyze the crystallographic structure of the as-prepared samples, and these results are illustrated in Fig. S1. After Ag NPs immersed into **Co-2TPABTz**, there is no distinct change in the **Co-2TPABTz** diffraction pattern, and all the major peaks belonged to Ag NPs are clearly identified [42]. No Ag₂O diffraction peaks are observed for composites **1–3**, because Ag NPs is absolutely coated with the help of **Co-2TPABTz** [43]. However, the Ag core has undergone partially oxidation since the content of Ag NPs is over 15 wt%.

The geometrical structure of composite **3** was elucidated by transmission electron microscope (TEM), high-resolution transmission electron microscope (HR-TEM) and selected-area electron diffraction (SAED) pattern characterizations (Fig. 1). A panoramic view (Fig. 1a) of composite **3** reveals that it is entirely composed of Ag NPs about uniform size. Lateral sizing histograms (Fig. S2) as well as additional TEM micrographs (Fig. 1b and c) display a core-shell structure consisting of a crystalline core of Ag NPs with a shell layer of **Co-2TPABTz** [44,45]. The average diameter of the Ag NPs is 3.4 nm and the surface **Co-2TPABTz** layer is about 2 nm, which may be the critical size in the composite system [46,47]. It is also demonstrating the incorporation of Ag nanocrystals into the porous **Co-2TPABTz** framework [13,48]. Meanwhile, from Fig. S2, it is found that critical particle sized Ag NPs (around 3.4 nm)

was embedded in **Co-2TPABTz** show excellent photocatalysis after-mentioned. This HR-TEM (Fig. 1c) presents the loaded Ag QDs (111) planes that have an inherent spacing distance of 0.237 nm [43]. And the d-spacing of 0.386 nm was assigned to the (021) facet of **Co-2TPABTz** in the same image [49]. From Fig. 1d, the SAED pattern displays several diffraction rings, which is the sum of diffraction patterns of Ag NPs and **Co-2TPABTz**. Among them, the diffraction rings of (111) and (200) are clearly observed, indicative of good crystallinity for Ag NPs [50]. It also contains another plane (021) matching with that of **Co-2TPABTz** [11,49]. Besides, the EDX data of the catalyst **3** showed that it mainly consists of C, O, S, N, Co and Ag (Fig. 1e). This manifests that Ag NPs are around with **Co-2TPABTz** evenly, which is identical with the elemental mapping patterns [43]. The TEM/HR-TEM observation, electron diffraction and EDX data confirm that the nanoporous matrix is composed of **Co-2TPABTz** and the embedded Ag NPs.

The ICP-AES data demonstrate that the desired Ag NPs loading on **Co-2TPABTz** varies between 1 and 20 wt% (Table 1). A similar tendency was observed for samples **1–5**, whose quantum yields (Φ) are summarized in Table 1 [11,51]. Sample **3** gives a stronger fluorescence. Moreover, the textural properties of these samples were evaluated by N₂ adsorption at 77 K and presented in Table 1. As synthesized with additional Ag NPs source, the S_{BET} of composites **1–5** ranges from 108.3 to 170.5 m² g^{−1}, a reflection of a typical mesoporous microstructure [14]. As expected, a marked increase to a certain degree was found in surface area when Ag NPs is introduced. The **Co-2TPABTz** loaded with Ag QDs (10 wt%) has the largest specific surface area. When the Ag NPs content was over 15 wt%, the S_{BET} of composites **4** and **5** progressively decreased due to the excessive agglomeration. In the meantime, as shown in Fig. S2 and Table 1, the grain sizes of composite **1–5** were between 3.4 and 11.7 nm. It can be observed that Ag NPs have been obtained with narrow size distributions [20]. This study indicates that the porous structure facilitate the separation of photo-generated electron-hole pairs [52].

XPS analysis was used to investigate the chemical compositions of the catalyst **3**. On the basis of the survey spectra for the composite **3**, there are six peaks located at 929.4, 573.8, 532.3, 400.5, 289.6 and 163.7 eV, which can be corresponding with (Co 2s), (Ag 3p), (O 1s), (N 1s), (C 1s) and (S 2p), respectively, indicating the high purity of as-prepared samples [44]. To further analyze the chemical nature of composite **3**, the high-resolution XPS spectra was examined and depicted in Fig. S3. It illustrated four prominent peaks at 367.6 eV, 373.8 eV, 780.4 eV and 794.6 eV, which are separately assigned to Ag (3d_{5/2}), Ag (3d_{3/2}), Co (2p_{3/2}), and Co (2p_{1/2}), evidencing that the successful fabrication of cobalt complex on the Ag NPs support in the composite **3** system [53].

To gain more insights into the charger carrier kinetics and the recombination of electrons/holes, time-resolved photoluminescence (TRPL) spectroscopy was performed on **Co-2TPABTz** and the responding composites **1–5**. The plots were further fitted with a biexponential function to generate two lifetime components, and these data are referred to individually as a fast (τ_1) and a slow (τ_2) decay (Table 2). Both decay components of those composites **1–5** were lengthened by the Ag NPs sensitizing [17]. A longer decay lifetime clearly reveals that lower recombination and higher separation efficiency of electron-hole pairs, leading to weaker photoluminescence and higher photocatalytic activity. It also suggests that the Ag NPs provide extra nonradiative pathways for charge transfer. Moreover, the charge trapping ability can be promoted by increasing the Ag NPs concentration [54].

To probe into the structure of **Co-2TPABTz** and composite **3**, the Raman spectra was carried out and elucidated in Fig. S4. The Raman spectra of **Co-2TPABTz** exhibited two remarkable peaks at around 610 and 1590 cm^{−1}, which belonged to the ν (Co–O) and ν (C=C) bands, separately [55]. Upon the integration of Ag NPs onto the **Co-**

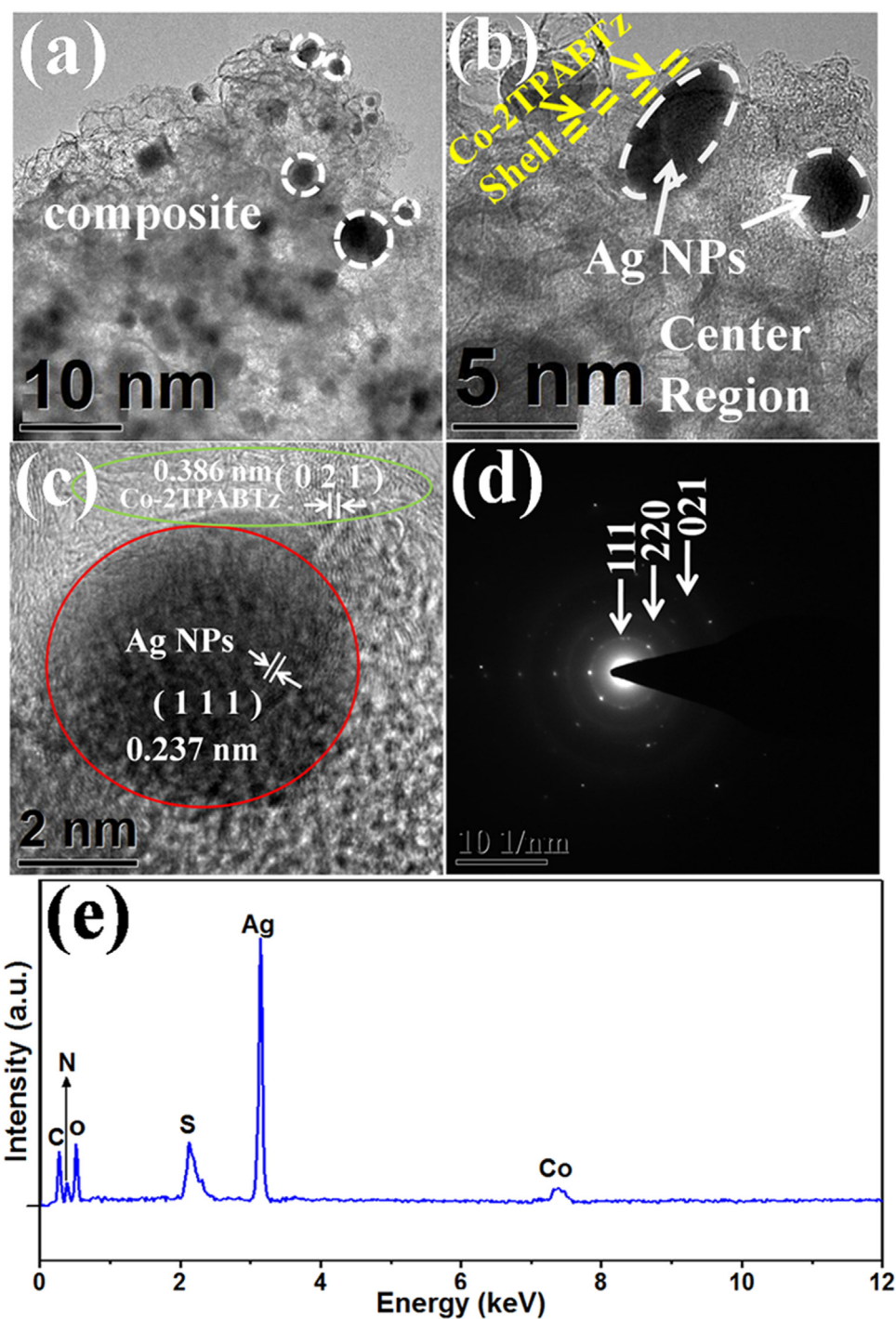


Fig. 1. TEM (a, b), HR-TEM (c) micrographs, SEAD pattern (d) and EDX spectra (e) of composite 3.

Table 1
Physicochemical properties of Co-2TPABTz and composites 1–5.

Sample	Ag NPs (wt%) nominal	Ag NPs (wt%) (ICP-AES)	Φ (%) ^a	S_{BET} ($\text{m}^2 \text{g}^{-1}$) ^b	Grain size (nm) ^c
1	1	1.2	74.3	149.2	7.5
2	5	5.6	82.1	158.4	5.9
3	10	10.1	91.4	170.5	3.4
4	15	15.3	66.5	143.7	9.8
5	20	20.4	60.2	108.3	11.7
Co-2TPABTz [13]	–	–	49.1	31.5	18.2

^a The solid fluorescence quantum yields (Φ) were determined by calibrated integrating sphere system ($\lambda_{\text{ex}} = 415 \text{ nm}$).

^b Measured from N_2 sorption studies.

^c Measured from DLS studies.

Table 2

The fluorescence lifetime, hydrogen production rate and AQY of the as-prepared photocatalysts.

Sample	τ_1 (ns) ^a	τ_2 (ns) ^a	H ₂ (mmol h ⁻¹ g ⁻¹) ^b	AQY (%) ^c
1	6.78	24.07	16.99	5.26
2	7.15	27.01	18.27	5.81
3	8.03	29.35	20.65	6.15
4	5.51	21.28	15.14	4.61
5	4.74	16.14	10.42	3.88
Co-2TPABTz [13]	2.01	–	0.46	0.14

^a Fluorescence lifetime.

^b Photocatalytic reaction was carried out over a 300 W Xe arc lamp using an ultra-violet cut-off filter; each catalyst (0.05 g) was dispersed under the above conditions.

^c AQY was obtained from the amounts of H₂ generated under mono-chromatic light irradiation ($\lambda = 420$ nm) in 1 h.

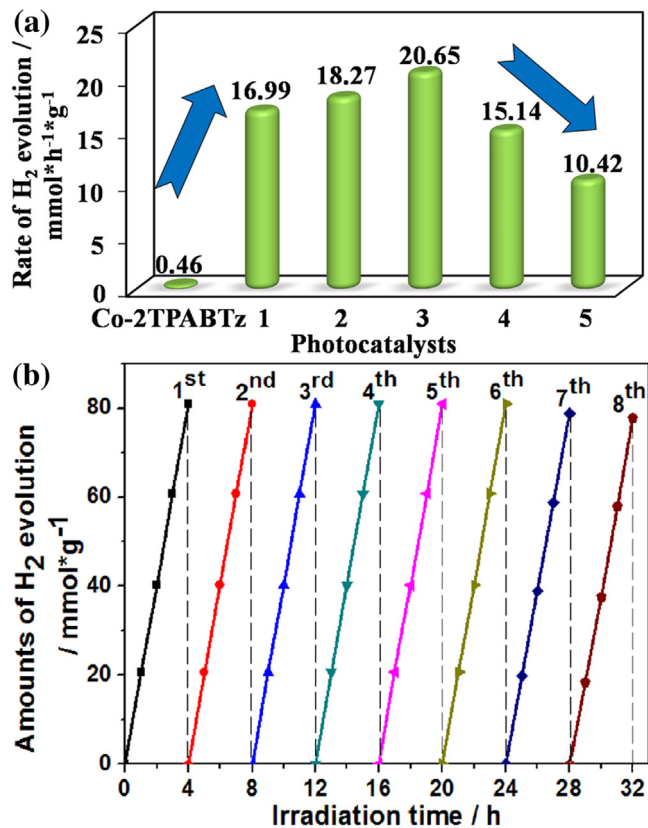


Fig. 2. Photocatalytic activity of the investigated samples (0.05 g) in an aqueous solution (100 mL) containing LA (10 mL) under visible-light illumination ($\lambda > 420$ nm): (a) comparison of the photocatalytic activities for Co-2TPABTz and the corresponding composites 1–5; (b) recyclability of the catalyst 3 (10 wt% Ag NPs) was continued for 32 h with evacuation every 4 h (dotted vertical lines).

2TPABTz, these two bands of composite 3 have become red-shifted and widened (from 610 cm⁻¹ to 630 cm⁻¹ and from 1590 cm⁻¹ to 1615 cm⁻¹), which might be ascribed to the interaction between Co-2TPABTz and Ag NPs by the disordered sp² carbon phase [56]. It is also a proof that the added Ag NPs were immobilized into Co-2TPABTz in the composite 3, which is well coincided with the previous TEM results.

3.2. Photocatalytic activity

Photocatalytic hydrogen evolution over different Ag NPs loaded Co-2TPABTz samples was evaluated under visible light irradiation ($\lambda > 420$ nm) using lactic acid (LA) as sacrificial agent, and shown in Fig. 2a. According to control experiments, no H₂ generation is observed at the present of either a catalyst or illumination [51,57].

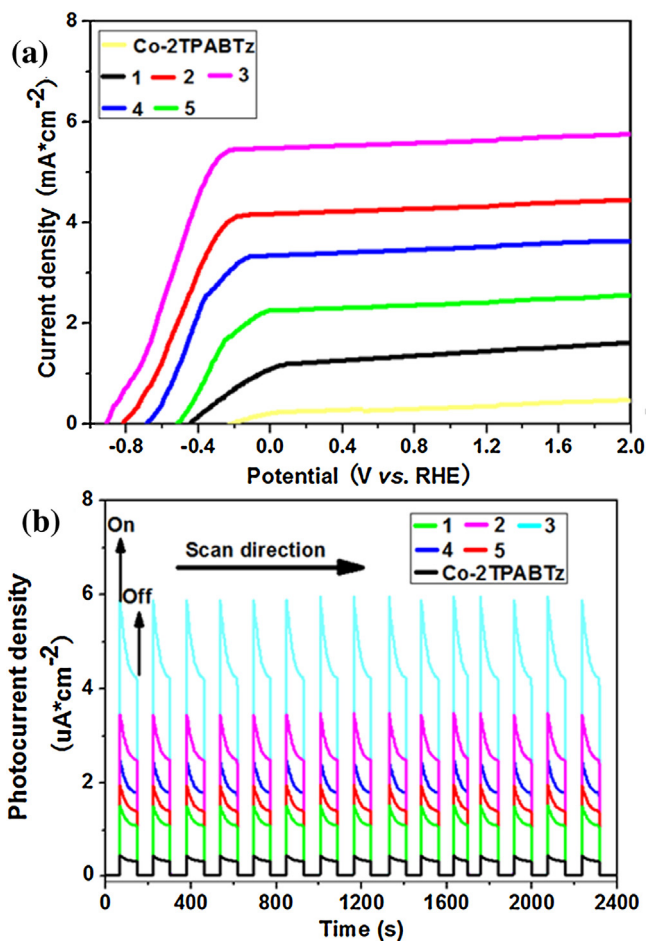


Fig. 3. (a) LSV of Co-2TPABTz and the as-synthesized samples 1–5; (b) transient photocurrent responses of Co-2TPABTz and the corresponding composites 1–5 with on-off cycles (32 h) under visible light illumination.

When using pure Co-2TPABTz as the photocatalyst, the rate of H₂ evolution was only 0.46 mmol h⁻¹ g⁻¹ (Table 2) [13]. Significantly, the rate of H₂ evolution increases for the Ag NPs-treated samples 1–5 as summarized in Table 2. This confirms the enhancement effects of the Ag NPs photosensitizer [58]. When the content of Ag NPs was 1 wt% in the composite 1, it exhibited a highly enhanced H₂ generation rate of 16.99 mmol h⁻¹ g⁻¹. In addition, a maximum one (20.65 mmol h⁻¹ g⁻¹) is obtained for composite 3, and its rate exceeds dramatically that of pure Co-2TPABTz. This corresponded to an AQY of 6.15% measured at 420 nm [2,59]. It might be attributed to the synergistic effects of the unique porous structure of Co-2TPABTz and strong SPR effect of Ag NPs, but also a heterojunction consisted of Ag NPs and Co-2TPABTz [60–62]. Afterwards, the H₂ generation rate reversely reduced with the amount of Ag NPs up to 15 wt%. This can be owing to more hole-electron recombination in the composite 4 and 5 [63].

Due to its outstanding photocatalytic activity, the reusability of composite 3 was investigated. The additional photocatalytic experiments were carried out in a 32 h duration without any recovery treatment over visible light ($\lambda > 420$ nm). As shown in Fig. 2b, it exhibits remarkable stability, and no obvious decrease in the H₂ generation rate was observed after eight consecutive cycles [11,22]. In the subsequent XRD (Fig. S5) and high-resolution XPS measurements (Table S1), the catalyst 3 can be separated easily and also keep unchangeable. Especially, the HR-XPS data (Table S1) show that there is no great change in the Ag 3d spectra before and after photocatalysis, indicating that Ag NPs in the composite 3 has good stability during photocatalytic reactions [64].

Apart from that, Fig. S6 displays the AQY for composite **3** at different incident light wavelengths. The AQY decreases with increasing wavelength, and the longest wavelength is suited to overall water splitting, in accordance with the DRS spectra of photocatalyst **3** [17]. It is noted that the photocatalytic reaction proceeds through light absorption [63].

3.3. Photoelectrochemical performance

From another point of view, current density-voltage (*J*-*V*) characteristics of **Co-2TPABTz** and hybrids **1–5** were measured under visible light irradiation and illustrated in Fig. 3a [65]. The photocurrent of bare **Co-2TPABTz** electrodes was negligible. Nevertheless, after the Ag NPs were directly loaded on the **Co-2TPABTz**, the photocurrent density of those composites **1–5** increased with increasing bias potential ranging from -1.0 V to 2.0 V as a result of the improved distribution of the Ag NPs for the effective separation of the photogenerated electron-hole pairs [66]. This confirms that Ag NPs deposition can prolong the lifetime of the photogenerated carriers [58]. Notably, the highest value was observed for 10 wt% Ag NPs in the composite **3**, which is about nearly 9-fold higher than that of **Co-2TPABTz**. But without visible-light illumination, their photocurrent densities have gone down to nearly zero, declaring that all the samples are inactive toward the photocatalytic reaction under dark conditions (Fig. S7) [30].

With **Co-2TPABTz** and the corresponding composites **1–5** as electrodes, respectively, the transient photocurrent responses were recorded for several on-off cycles under simulated visible light illumination ($\lambda > 420$ nm) vs. RHE bias potential [29]. As shown in Fig. 3b, all the photocatalysts displayed prompt and reproducible photocurrent, those composites exhibited stronger photocurrents compared with **Co-2TPABTz**. Along with the content of Ag NPs added to 10 wt%, composite **3** photoelectrode reached the highest one. This great heightening in the photocurrent output, leading to efficient separation of photo excited electron-hole pairs, and thus increases the photocatalytic stability [64,67]. Therefore, it implies that composite **3** definitely has the best stability among them in photocatalytic H_2 production. Whereas a decrease of photocurrent density was given in excess of 15 wt% Ag NPs for other composites. The reason may be that much more Ag NPs accumulated in the system, shielding the active sites, resulting in lower optical absorption for the hybrid [65].

Subsequently, prolonged photocurrent tests are applied to determine the stability of the composite **3**, as illustrated in Fig. S8. The photocurrent started to decrease, possibly ascribing to the photo-oxidation or photocorrosion that occurred on the composite **3** through accumulated photoinduced holes [31], and then it kept up a steady trend under visible-light irradiation [60]. Noticeable, it exhibited outstanding long-term operation stability beyond 32 h, which was in agreement with the previous XRD and high-resolution XPS analysis [30,65].

In addition to understanding the charge transfer process, the measurement of electrochemical impedance spectroscopy (EIS) was conducted as well. Fig. 4 demonstrates EIS Nyquist plots of all the tested photoelectrode samples **1–5** and **Co-2TPABTz**. Via comparison of the different samples, composite **3** exhibited the smallest arch diameter, which suggested the fastest interfacial electron transfer [68]. Similarly, combining with Ag NPs could effectively accelerate the electron mobility by suppressing the recombination of photo-generated carriers [69]. It was noted that Ag NPs played an important role in the solution-action process of electron transfer [23].

On the other hand, electron spin resonance (ESR) spectra of **Co-2TPABTz** and those composites **1–5** were carried out under vacuum conditions (Fig. S9). The higher vibration peak from the ESR spectra displays that the longer life time of free electrons, that

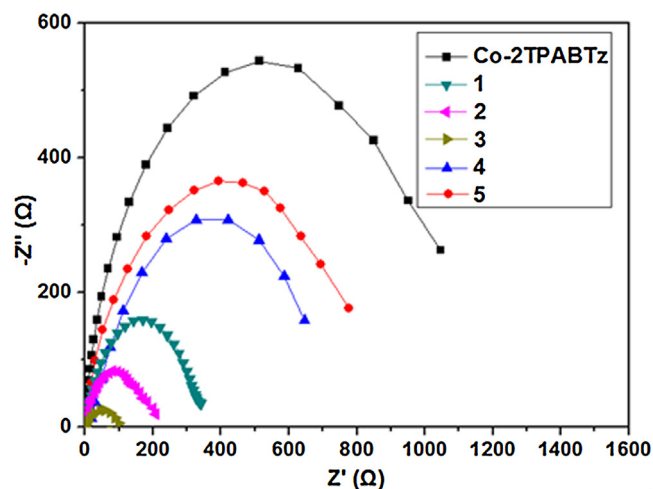


Fig. 4. EIS Nyquist plots of **Co-2TPABTz** and the as-synthesized samples **1–5**.

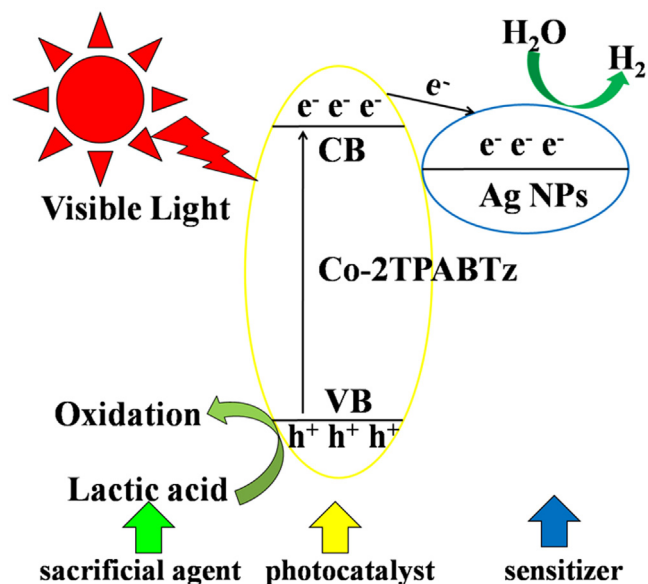


Fig. 5. Schematic illustration of charge separation and transfer in the catalyst **3** under visible-light illumination.

is, the recombination of holes and electrons has been prevented [14]. As demonstrated by Fig. S9, the intensity of the vibration for **Co-2TPABTz** is rather lower, and increases for those composites. Among the as-synthesized composites, the intensity of the vibration for composite **3** is the strongest one, as a reflection of the best suppression of the recombination. It also elucidates that the Ag NPs is beneficial for transfer of the photo-generated electrons, and contribute to the proton reduction in the consequent photocatalytic reaction [21]. Besides, the ESR spectra of composite **3** before visible-light illumination under vacuum or the atmosphere are shown in Fig. S9g. It is not surprising that there exists no signal for composite **3** in the absence of visible light. The intensity of photo-generated ESR signal is in accordance with the above-mentioned photocatalytic activity.

3.4. Possible photocatalytic mechanism

Based on the above results, the mechanism for the photocatalytic H_2 evolution over catalyst **3** is proposed (Fig. 5). Upon visible-light illumination, the electrons (e^-) in the valence band (VB, Table S2) of **Co-2TPABTz** are excited to the conduction band

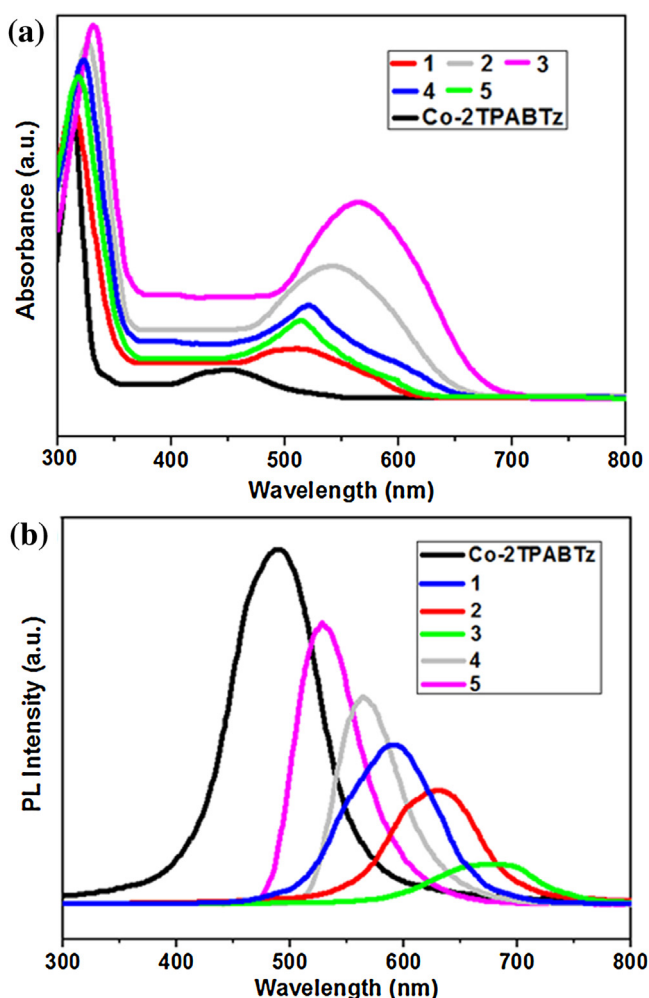


Fig. 6. UV-vis (a) and PL (b) spectra of Co-2TPABTz and the corresponding composites 1–5.

(CB, Table S2), leaving behind holes (h^+) in the VB. Simultaneously, the energy levels of the CB and VB edges (Table S2) assure that redox Ag NPs act as sensitizers, which makes Co-2TPABTz highly active under visible light [58]. Owing to the collective oscillations of the surface electrons, Ag NPs can arouse the SPR effect in the system [23,50]. The SPR of Ag NPs locates at the visible light region, making a contribution to the rapid capture and steady transportation of photo-generated electrons [5]. Meanwhile, the positive holes are mainly consumed by lactic acid [56].

3.5. Optical property

To verify the upper mechanism, UV-vis spectra of various samples are demonstrated in Fig. 6a, respectively. Their UV-vis spectra featured the most intense absorption bands in the ultraviolet region at wavelengths below 330 nm, arising from the $\pi-\pi^*$ transition for the bithiazole ligand [13]. The bare Co-2TPABTz exhibited an MLCT band at 440 nm with an intense transition in the visible-light region [5,70]. While the strong and broad absorption band of those samples 1–5 further approach the visible-light region, ascribing to the photosensitizing and SPR effect of Ag NPs [18,54]. It is well-known that pure Ag NPs exhibit SPR absorption at about 400 nm [71], while this peak cannot be observed in this system due to the optical cutoff from the Co-2TPABTz substrate [72,73].

In another case, the enhanced photocatalytic activity for H_2 generation is probably attributed to the fast interfacial trans-

fer of photogenerated charge carriers between Co-2TPABTz and Ag NPs and subsequent effective charge separation [29]. The photo-induced charge transfer was confirmed by PL spectra of the semiconductor composites, as presented in Fig. 6b. The PL spectra were measured at room temperature for Co-2TPABTz and the corresponding composites 1–5. The pure Co-2TPABTz sample exhibits a strong emission peak centered at 490 nm. In contrast, the PL intensity of other composites was obviously quenched and red-shifted, indicating an efficient photoinduced charge transfer process between Co-2TPABTz and Ag NPs [63,74]. A slight red shift of the emission peak compared with Co-2TPABTz was mainly ascribed to the wrapping with Ag NPs quenching the fluorescence from Co-2TPABTz, the energy of emission light is reductive than that of Co-2TPABTz, and the charge carrier transformation between Co-2TPABTz and Ag NPs [75]. The lowest PL intensity was observed for the composite 3, suggesting that the Ag NPs photosensitizer helps the transfer of charge carriers and slows down the recombination process [51].

On the basis of all the results, it can be claimed this novel composite 3 possesses several attractive features in comparison to other photocatalysts, including facile, simplicity, high stability, excellent photocatalytic performance and practicality. For example: sophisticated preparation process is not required, photocatalytic activity is remained within 8 cycles, and the visible light induced photocatalytic H_2 generation [22]. As given in Table S3, the substitution of Cu or C_{60} with Ag NPs in the composite will bring about further improvement in photocatalysis efficiency [13,25]. Although more mechanistic studies are further needed to establish and better understand photophysical and catalytic properties of the Co-complex composites, these findings of the present study provide new minds into the development of the integration of Co-complex with Ag NPs to exploit numerous potential applications [12,23]. Further application research using this new cobalt complex-based photocatalyst, such as water purification and direct methanol fuel cells, is now going on in our laboratory [13].

4. Conclusion

In summary, a series of Co-2TPABTz composite photocatalysts have been successfully synthesized and characterized systematically. They demonstrated extraordinarily enhancement in the photocatalytic activity toward hydrogen production under visible light illumination as well. Overall, the composite 3 containing 10 wt% Ag NPs achieved for the highest one ($20.65 \text{ mmol h}^{-1} \text{ g}^{-1}$). The heightening photocatalytic activity was ascribed to the synergistic effects of the unique porous structure of Co-2TPABTz and strong SPR effect of Ag NPs. This new composite is not only an emerging class of material that clearly has a bright future, but also the potential for contributions across several fields of applied research.

Acknowledgments

We are grateful to the National Natural Science Foundation of China (No. 21571064, 21371060) and the research fund of the Key Laboratory of Fuel Cell Technology of Guangdong Province for financial support. We thank Benjamin J. Deibert for proofreading this article.

Appendix A. Supplementary data

Supplementary data associated with this article can be found, in the online version, at <http://dx.doi.org/10.1016/j.apcatb.2016.06.047>.

References

- [1] N.S. Lewis, *Science* (2016), <http://dx.doi.org/10.1126/science.aad1920>, in press.
- [2] J. Willkomm, K.L. Orchard, A. Reynal, E. Pastor, J.R. Durrant, E. Reisner, *Chem. Soc. Rev.* 45 (2016) 9–23.
- [3] Q.P. Lu, Y.F. Yu, Q.L. Ma, B. Chen, H. Zhang, *Adv. Mater.* 28 (2016) 1917–1933.
- [4] V.S. Vyas, B.V. Lotsch, *Nature* 521 (2015) 41–42.
- [5] Y.G. Chen, S. Zhao, X. Wang, Q. Peng, R. Lin, Y. Wang, R.A. Shen, X. Cao, L.B. Zhang, G. Zhou, J. Li, A.D. Xia, Y.D. Li, *J. Am. Chem. Soc.* 138 (2016) 4286–4289.
- [6] M.M. Najafpour, G. Renger, M. Holyńska, A.N. Moghaddam, E.-M. Aro, R. Carpentier, H. Nishihara, J.J. Eaton-Rye, J.-R. Shen, S.I. Allakhverdiev, *Chem. Rev.* 116 (2016) 2886–2936.
- [7] J. Liu, Y. Liu, N.Y. Liu, Y.Z. Han, X. Zhang, H. Huang, Y. Lifshitz, S.-T. Lee, J. Zhong, Z.K. Kang, *Science* 347 (2015) 970–974.
- [8] R.S. Sprick, B. Bonillo, R. Clowes, P. Guiglion, N.J. Brownbill, B.J. Slater, F. Blanc, M.A. Zwijnenburg, D.J. Adams, A.I. Cooper, *Angew. Chem.* 55 (2016) 1792–1796.
- [9] A. Schoedel, Z. Ji, O.M. Yaghi, *Nat. Energy* 1 (2016) 16034–16046.
- [10] Y.C. Simon, C. Weder, *Nat. Mater.* 14 (2015) 864–865.
- [11] Z.-L. Wu, C.-H. Wang, B. Zhao, J. Dong, F. Lu, W.-H. Wang, W.-C. Wang, G.-J. Wu, J.-Z. Cui, P. Cheng, *Angew. Chem. Int. Ed.* 55 (2016) 4938–4942.
- [12] J. Aguilera-Sigalat, D. Bradshaw, *Coord. Chem. Rev.* 307 (2016) 267–291.
- [13] J.P. Huo, H.P. Zeng, *J. Mater. Chem. A* 3 (2015) 6258–6264.
- [14] V.P. Santos, T.A. Wezendonk, J.J.D. Jaén, A.I. Dugulan, M.A. Nasalevich, H.-U. Islam, A. Chojecki, S. Sartipi, X.H. Sun, A.A. Hakeem, A.C.J. Koeken, M. Ruitenbeek, T. Davidian, G.R. Meima, G. Sankar, F. Kapteijn, M. Makkee, J. Gascon, *Nat. Commun.* 6 (2015) 6451–6458.
- [15] M.C. Wen, K. Mori, Y. Kuwahara, H. Yamashita, *ChemCatChem* 7 (2016) 3519–3525.
- [16] M.D. Regulacio, M.-Y. Han, *Acc. Chem. Res.* 49 (2016) 511–519.
- [17] S. Bai, J. Jiang, Q. Zhang, Y.J. Xiong, *Chem. Soc. Rev.* 44 (2015) 2893–2939.
- [18] H. Robatjazi, S.M. Bahaiddin, C. Doiron, I. Thomann, *Nano Lett.* 15 (2015) 6155–6161.
- [19] J. Ryu, Y.J. Jang, S. Choi, H.J. Kang, H. Park, J.S. Lee, S. Park, *NPG Asia Mater.* 8 (2016) e248–e256.
- [20] Z.B. Zhan, F. Grote, Z.J. Wang, R. Xu, Y. Lei, *Adv. energy mater., Energy Mater.* (2016), <http://dx.doi.org/10.1002/aenm.201501654>, in press.
- [21] C.F. Tan, W.L. Ong, G.W. Ho, *ACS Nano* 9 (2015) 7661–7670.
- [22] M. Wang, K. Han, S. Zhang, L.C. Sun, *Coord. Chem. Rev.* 287 (2015) 1–14.
- [23] Z.C. Lian, W.C. Wang, S.N. Xiao, X. Li, Y.Y. Cui, D.Q. Zhang, G.S. Li, H.X. Li, *Sci. Rep.* 5 (2015) 10461–10470.
- [24] P.F. Smith, B.J. Deibert, S. Kaushik, G. Gardner, S. Hwang, H. Wang, J.F. Al-Sharab, E. Garfunkel, L. Fabris, J. Li, G.C. Dismukes, *ACS Catal.* 6 (2016) 2089–2099.
- [25] J.P. Huo, H.P. Zeng, *J. Mater. Chem. A* 3 (2015) 17201–17208.
- [26] J.P. Huo, L.T. Fang, Y.L. Lei, H.P. Zeng, *J. Mater. Chem. A* 2 (2014) 11040–11044.
- [27] I. Dóka, A. Bíró, Q. Johansson, K. Ballagó, J.R. Prigge, T.P. Pastor-Flores, E.E. Dick, E.S.J. Arnér, P. Nagy, *Sci. Adv.* (2016), <http://dx.doi.org/10.1126/sciadv.1500968>, in press.
- [28] Q.Q. Shi, K.J. Si, D. Sikdar, L.W. Yap, M. Premaratne, W.L. Cheng, *ACS Nano* 10 (2016) 967–976.
- [29] G.S. Li, Z.C. Lian, W.C. Wang, D.Q. Zhang, H.X. Li, *Nano Energy* 19 (2016) 446–454.
- [30] M. Cabán-Acevedo, M.L. Stone, J.R. Schmidt, J.G. Thomas, Q. Ding, H.-C. Chang, M.-L. Tsai, J.-H. He, S. Jin, *Nat. Mater.* 14 (2015) 1245–1251.
- [31] C.-J. Chen, K.-C. Yang, M. Basu, T.-H. Lu, Y.-R. Lu, C.-L. Dong, S.-F. Hu, R.-S. Liu, *ACS Appl. Mater. Interfaces* 8 (2016) 5400–5407.
- [32] A. Morais, C. Longo, J.R. Araujo, M. Barroso, J.R. Durrant, A.F. Nogueira, *Phys. Chem. Chem. Phys.* 18 (2016) 2608–2616.
- [33] M. Li, R.J. Zhao, Y.J. Su, Z. Yang, Y.F. Zhang, *Nanoscale* 8 (2016) 8559–8567.
- [34] Y. Ren, M. Sezen, F. Guo, F. Jäkle, Y.-L. Loo, *Chem. Sci.* 7 (2016) 4211–4219, <http://dx.doi.org/10.1039/C6SC00519E>.
- [35] I. Shown, H.-C. Hsu, Y.-C. Chang, C.-H. Lin, P.K. Roy, A. Ganguly, C.-H. Wang, J.-K. Chang, C.-I. Wu, L.-C. Chen, K.-H. Chen, *Nano Lett.* 14 (2014) 6097–6103.
- [36] Y.M. Yang, N.Y. Liu, S. Qiao, R.H. Liu, H. Huang, Y. Liu, *New J. Chem.* 39 (2015) 2815–2821.
- [37] R.H. Liu, H. Huang, H.T. Li, Y. Liu, J. Zhong, Y.Y. Li, S. Zhang, Z.H. Kang, *ACS Catal.* 4 (2014) 328–336.
- [38] W.-K. Jo, J.Y. Lee, T.S. Natarajan, *Phys. Chem. Chem. Phys.* 18 (2016) 1000–1016.
- [39] A. Sinhamahapatra, J.-P. Jeon, J.-S. Yu, *Energy Environ. Sci.* 8 (2015) 3539–3544.
- [40] C.Y. Duan, H. Wang, X.M. Ou, F. Li, X.H. Zhang, *ACS Appl. Mater. Interfaces* 6 (2014) 9742–9750.
- [41] J. He, L. Chen, F. Wang, Y. Liu, P. Chen, C.-T. Au, S.-F. Yin, *ChemSusChem* 9 (2016) 624–630.
- [42] K. Kirshenbaum, D.C. Bock, C.-Y. Lee, Z. Zhong, K.J. Takeuchi, A.C. Marschilok, E.S. Takeuchi, *Science* 347 (2015) 149–154.
- [43] D.J. Martin, G.G. Liu, S.J.A. Moniz, Y.P. Bi, A.M. Beale, J.H. Ye, J.W. Tang, *Chem. Soc. Rev.* 44 (2015) 7808–7828.
- [44] N.T. Nguyen, M. Altomare, J.E. Yoo, P. Schmuki, *Adv. Mater.* 27 (2015) 3208–3215.
- [45] B.C.M. Martindale, G.A.M. Hutton, C.A. Caputo, E. Reisner, *J. Am. Chem. Soc.* 137 (2015) 6018–6025.
- [46] Z.F. Jiang, J.M. Xie, *RSC Adv.* 6 (2016) 3186–3197.
- [47] Y. Choi, H.-i. Kim, G.-h. Moon, S. Jo, W. Choi, *ACS Catal.* 6 (2016) 821–828.
- [48] S. Lin, C.S. Diercks, Y.-B. Zhang, N. Kornienko, E.M. Nichols, Y.B. Zhao, A.R. Paris, D. Kim, P.D. Yang, O.M. Yaghi, C.J. Chang, *Science* 349 (2015) 1208–1213.
- [49] C. Bachmann, B. Probst, M. Oberholzer, T. Fox, R. Alberto, *Chem. Sci.* 7 (2015) 436–441.
- [50] C.-Y. Wang, H.-Y. Chen, L.Y. Sun, W.-L. Chen, Y.-M. Chang, H. Ahn, X.Q. Li, S. Gwo, *Nat. Commun.* 6 (2015) 7734–7740.
- [51] F. Núñez, L. Fresno, P. Collado, J.M. Jana, D.P. Serrano, V.A. de la Peña O'shea, *Appl. Catal. B* 191 (2016) 106–115.
- [52] X. Li, J.G. Yu, M. Jaroniec, *Chem. Soc. Rev.* 45 (2016) 2603–2636.
- [53] Y. Chen, P.D. Tran, P. Boix, Y. Ren, S.Y. Chiam, Z. Li, K.W. Fu, L.H. Wong, J. Barber, *ACS Nano* 9 (2015) 3829–3836.
- [54] N. Mondal, A. Samanta, *J. Phys. Chem. C* 120 (2016) 650–658.
- [55] N. Gao, X.S. Fang, *Chem. Rev.* 115 (2015) 8294–8343.
- [56] H.G. Yu, J. Tian, F. Chen, P. Wang, X.F. Wang, *Sci. Rep.* 5 (2015) 13083–13093.
- [57] Y. Ma, X.L. Wang, Y.S. Jia, X.B. Chen, H.X. Han, C. Li, *Chem. Rev.* 114 (2014) 9987–10043.
- [58] M.-Z. Ge, C.-Y. Cao, S.-H. Li, Y.-X. Tang, L.-N. Wang, N. Qi, J.-Y. Huang, K.-Q. Zhang, S.S. Al-Deyab, Y.-K. Lai, *Nanoscale* 8 (2016) 5226–5234.
- [59] S. Saha, G. Das, J. Thote, R. Banerjee, *J. Am. Chem. Soc.* 136 (2014) 14845–14851.
- [60] S.J.A. Moniz, S.A. Shevlin, D.J. Martin, Z.-X. Guo, J.W. Tang, *Energy Environ. Sci.* 8 (2015) 731–759.
- [61] K. Li, A.D. Handoko, M. Khraisheh, J.W. Tang, *Nanoscale* 6 (2014) 9767–9773.
- [62] J.W. Tang, J.R. Durrant, D.R. Klug, *J. Am. Chem. Soc.* 130 (2008) 13885–13891.
- [63] P.S. Kumar, J. Sundaramurthy, S. Sundarajan, V.J. Babu, G. Singh, S.I. Allakhverdiev, S. Ramakrishna, *Energy Environ. Sci.* 7 (2014) 3192–3222.
- [64] T.-F. Yeh, S.-J. Chen, H. Teng, *Nano Energy* 12 (2015) 476–485.
- [65] T.-T. Zhuang, Y. Liu, M. Sun, S.-L. Jiang, M.-W. Zhang, X.-C. Wang, Q. Zhang, J. Jiang, S.-H. Yu, *Angew. Chem. Int. Ed.* 54 (2015) 11495–11500.
- [66] T.P. Nguyen, S. Choi, J.-M. Jeon, K.C. Kwon, H.W. Jang, S.Y. Kim, *J. Phys. Chem. C* 120 (2016) 3929–3935.
- [67] Y.J. Zhang, B. Tang, Z.Y. Wu, H.J. Shi, Y.N. Zhang, G.H. Zhao, *Green Chem.* 18 (2016) 2424–2434.
- [68] H. Ren, H. Shao, L.J. Zhang, D. Guo, Q. Jin, R.B. Yu, L. Wang, Y.L. Li, Y. Wang, H.J. Zhao, D. Wang, *Adv. Energy Mater.* (2016), <http://dx.doi.org/10.1002/aenm.201500296>, in press.
- [69] X.X. Chang, T. Wang, P. Zhang, J.J. Zhang, A. Li, J.L. Gong, *J. Am. Chem. Soc.* 137 (2015) 8356–8359.
- [70] M.G. Kibria, F.A. Chowdhury, S. Zhao, B. Alotaibi, M.L. Trudeau, H. Guo, Z. Mi, *Nat. Commun.* 6 (2015) 6797–6804.
- [71] X.H. Li, J.M. Zhu, B.Q. Wei, *Chem. Soc. Rev.* 45 (2016) 3145–3187.
- [72] S. Peglow, M.-M. Pohl, A. Kruth, V. Brüser, *J. Phys. Chem. C* 119 (2015) 563–572.
- [73] W.Y. Gao, M.Q. Wang, C.X. Ran, X. Yao, H.H. Yang, J. Liu, D.L. He, J.B. Bai, *Nanoscale* 6 (2014) 5498–5508.
- [74] Z.J. Sun, X. Liu, Q.D. Yue, H.X. Jia, P.W. Du, *ChemCatChem* 8 (2016) 157–162.
- [75] M.J. Zhou, J.Z. Li, Z.F. Ye, C.C. Ma, H.Q. Wang, P.W. Huo, W.D. Shi, Y.S. Yan, *ACS Appl. Mater. Interfaces* 7 (2015) 28231–28243.